Article

Measurement-induced entanglement phase transition on a superconducting quantum processor with mid-circuit readout

Jin Ming Koh ⓘ[1], Shi-Ning Sun[2], Mario Motta[3] & Austin J. Minnich ⓘ[2] ✉

Quantum many-body systems subjected to unitary evolution with the addition of interspersed measurements exhibit a variety of dynamical phases that do not occur under pure unitary evolution. However, these systems remain challenging to investigate on near-term quantum hardware owing to the need for numerous ancilla qubits or repeated high-fidelity mid-circuit measurements, a capability that has only recently become available. Here we report the realization of a measurement-induced entanglement phase transition with a hybrid random circuit on up to 14 superconducting qubits with mid-circuit readout capability. We directly observe extensive and sub-extensive scaling of entanglement entropy in the volume- and area-law phases, respectively, by varying the rate of the measurements. We also demonstrate phenomenological critical behaviour by performing a data collapse of the measured entanglement entropy. Our work establishes the use of mid-circuit measurement as a powerful resource for quantum simulation on near-term quantum computers.

Ergodic quantum many-body systems undergoing unitary dynamics evolve towards increasingly entangled states characterized by an extensive scaling of entanglement entropy with system volume[1–6]. At the other extreme, quantum systems that are repeatedly measured may be stabilized in a measurement eigenstate, a phenomenon known as the quantum Zeno effect[7–10]. The intermediate regime in which unitary evolution is interspersed with quantum measurements has recently garnered interest[11–14]. Numerical studies have reported the existence of distinct phases characterized by volume- and area-law entanglement entropy scaling for infrequent and frequent measurement rates, respectively, separated by a critical measurement rate at which a phase transition occurs[15–20].

This phenomenon of measurement-induced entanglement transitions stems from a competition between unitary evolution and quantum measurements, which respectively generate and destroy entanglement[15–17]. The distinct phases are illustrated schematically in Fig. 1a. On quantum circuits containing random unitaries, we consider a measurement rate per time step $p \in [0, 1]$, corresponding to the probability of performing a measurement on each qubit, and a measurement strength $\eta \in [0, 1]$, defined using the degree of entanglement with an ancilla qubit that is projectively measured[21–23]. Measurements are effectively projective on the system qubit at $\eta = 1$ and have no effect at $\eta = 0$. At low p or η, beginning from a separable state, ballistic growth in the entanglement entropy of a subsystem with time first occurs, eventually plateauing to a steady-state value that scales extensively with the system size. A sufficiently large p or η, however, can suppress entanglement. In such a regime, no ballistic growth occurs, and the steady-state entanglement entropy scales sub-extensively. These dynamical features and, in particular, scaling of the steady-state value of entanglement entropy with subsystem size, characterize the volume- and area-law phases, respectively.

Under projective measurements ($\eta = 1$), in the thermodynamic limit of infinite system size, a sharp entanglement transition has been found to occur at a critical measurement rate p^* separating the area-law and volume-law phases[15–20]. Near the transition, the entanglement entropy scales logarithmically with system size to leading order[15–17].

[1]Division of Physics, Mathematics and Astronomy, California Institute of Technology, Pasadena, CA, USA. [2]Division of Engineering and Applied Science, California Institute of Technology, Pasadena, CA, USA. [3]IBM Quantum, IBM Research Almaden, San Jose, CA, USA. ✉e-mail: aminnich@caltech.edu
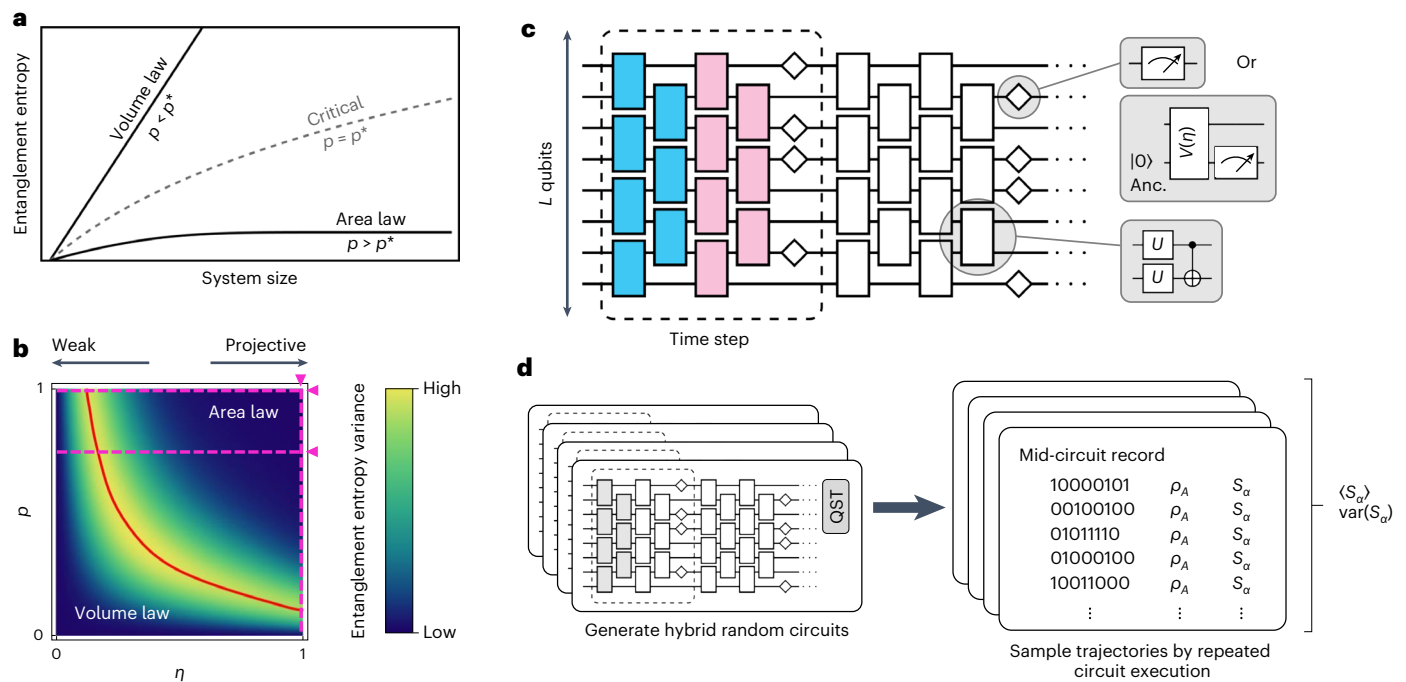
Fig. 1 | Measurement-induced entanglement transition using a hybrid random quantum circuit model. a, Schematic of entanglement entropy versus system size, illustrating the various measurement-induced phases. Under projective measurements ($\eta = 1$), an entanglement transition occurs at a critical measurement rate p^*, separating a volume-law phase for $p < p^*$ and an area-law phase for $p > p^*$. Entanglement entropy scales extensively and sub-extensively, respectively, in these two phases. **b**, Qualitative diagram of steady-state entanglement entropy variance in p–η space, exhibiting a ridge that separates volume- and area-law regimes. Dashed magenta horizontal and vertical lines mark the parameter sweeps probed in this study. **c**, Structure of random quantum circuits employed in this work, comprising several time steps. Each time step consists of two layers (dark blue and light pink) of randomized

two-qubit gates in a brickwork pattern and a layer of measurements randomly placed on each qubit with probability p. The measurements can be projective, or weak with strength η, achieved through coupling with an ancillary qubit (Anc.). Each two-qubit gate comprises random single-qubit rotations and a randomly directed CX. **d**, Overview of experimental methodology. At a chosen (p, η), a set of hybrid random quantum circuits is generated and executed repeatedly on quantum hardware. The reduced density matrix ρ_A of a subsystem A for each trajectory, defined by the mid-circuit measurement bitstring, is recovered through QST, and the entanglement entropy S_α is computed. Finally, the mean entanglement entropy $\langle S_\alpha \rangle$ and variance $\mathrm{var}(S_\alpha)$ are calculated over all trajectories and circuit samples (Methods).

The volume- and area-law phases manifest at $p < p^*$ and $p > p^*$, respectively. It has been proposed that the crossover between the two phases could be identified by a ridge of increased entanglement entropy variance in p–η parameter space, as the system fluctuates between entanglement growth and suppression (see Fig. 3 of ref. [18]), as schematically illustrated in Fig. 1b. Other signatures of the transition have also been considered using measures of entanglement such as bipartite and tripartite mutual information[16,17,19,24]. A variety of models exhibiting entanglement transitions have so far been studied numerically, including random quantum circuits with local Clifford and Haar unitaries[16–19] and higher-dimensional connectivity[17,20,25,26], interacting bosonic and spin chains[27,28] and symmetric circuits supporting topological phases[29]. Theoretical connections to quantum error correction[30–32] and conformal field theory[33–37], concerning the stability of the phases and criticality, have also been uncovered. In contrast to dissipative phenomena in open quantum systems, measurement-induced phase transitions are not apparent from the density matrix of the system averaged over measurement outcomes, but instead require the resolution of individual quantum trajectories[14–17].

Experimentally realizing these dynamic quantum phases of matter and the transition between them on near-term quantum hardware is difficult due to the need for repeated high-fidelity mid-circuit measurements (≥ 10) over non-trivial system sizes (≥ 10 qubits). Although the evolving unitaries are random, fine control over their distribution and entangling properties is necessary to identify the quantum phase transition while avoiding confounding entropy contributions (Supplementary Note 7). In a recent work on a trapped-ion quantum

computer, a purification phase transition, expected to occur concurrently with entanglement phase transitions[34,38] was observed using Clifford circuits and deferred measurements[39]. However, the feedback approach circumventing post-selection does not efficiently generalize to non-stabilizer circuits, and the ancillary qubit overhead incurred by the deferred measurements complicated the investigation of larger system sizes. More generally, the use of hybrid quantum circuits in which mid-circuit measurement is exploited to reduce quantum resource requirements has been only minimally explored[40,41].

Entanglement in hybrid random quantum circuits on hardware

We probed a volume- to area-law entanglement phase transition on a non-Clifford random circuit model with up to 14 qubits by leveraging recent hardware advances in superconducting quantum computers, particularly the ability to perform sub-microsecond (~750 ns) mid-circuit measurements[40]. Our experiments spanned ~5,200 hardware device-hours (~32,000 qubit-hours) over multiple quantum processors, making them among the most resource-intensive quantum simulations on near-term hardware reported (see Supplementary Note 1 for further details).

The hybrid random circuit model used to realize measurement-induced entanglement transitions is shown in Fig. 1c. The experiment circuits comprised interleaved unitary entangling layers and mid-circuit measurements on a 1D qubit chain, repeated over several time steps. Unlike in previous experimental works that probed measurement-induced phase transitions, measurements were not
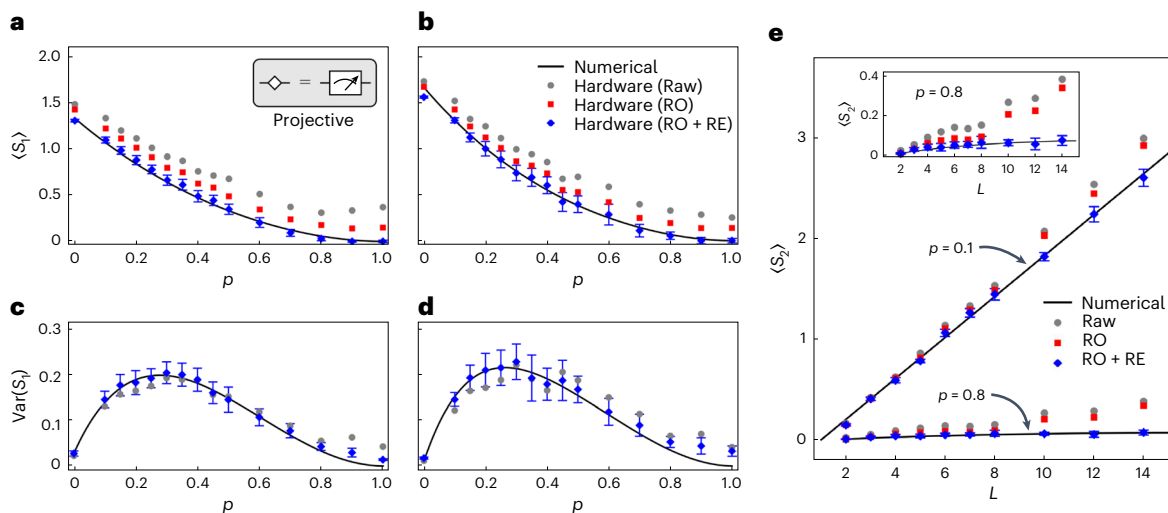
Fig. 2 | Entanglement crossover and system size scaling under projective measurements. a–d, $\langle S_1 \rangle$ versus p at system sizes $L = 4$ (**a**) and $L = 5$ (**b**), and S_1 variance versus p at system sizes $L = 4$ (**c**) and $L = 5$ (**d**) obtained on quantum hardware at subsystem sizes $|A| = \lfloor L/2 \rfloor$ with readout error mitigation (RO) and residual entropy correction (RE), shown as blue diamonds. Projective measurements ($\eta = 1$) were used, as indicated by the inset icon in **a**. Raw hardware data (grey dots), data with RO applied (red squares) and ideal noiseless numerical results without sampling (solid line) are shown for comparison. Excellent agreement between hardware data with RO and RE applied and ideal entropies is observed. **e**, $\langle S_2 \rangle$ versus L for up to $L = 14$ qubits obtained on hardware. At $p = 0.1 < p^*$, the system exhibits volume-law behaviour and entanglement entropy is linearly proportional to system size, whereas at high $p = 0.8 > p^*$ the system exhibits area-law scaling and the entanglement entropy saturates. Inset: zoomed-in plot of $\langle S_2 \rangle$ versus L for $p = 0.8$ data. Quantum devices {ibm_lagos, ibm_perth, ibmq_jakarta, ibmq_casablanca} were used for $L \le 5$, and {ibm_hanoi, ibm_cairo, ibm_kolkata, ibm_auckland, ibm_washington} with sub-microsecond readout were used for $L > 5$. Error bars reflect 90% confidence intervals estimated from statistical bootstrapping.
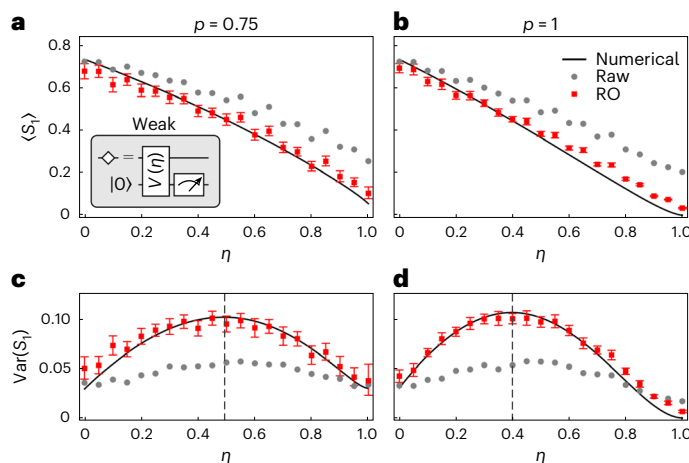

Fig. 3 | Entanglement crossover under weak measurements. a–d, $\langle S_1 \rangle$ versus η (**a,b**) and S_1 variance (**c,d**) at $p = 0.75$ (**a,c**) and $p = 1$ (**b,d**) versus η obtained on quantum hardware at $L = 3$ and $|A| = 1$. Hardware data with RO applied (red squares), raw data (grey dots) and ideal noiseless numerical results without sampling (solid line) are shown. The location of the crossover (vertical dashed line) is now dependent on p. Quantum devices {ibmq_guadalupe, ibmq_montreal} were used. Error bars reflect 98% confidence intervals estimated from statistical bootstrapping. Inset schematic in **a** illustrates the implementation of weak measurements through coupling to an ancillary qubit (Methods).

deferred. The unitary layers contained randomized two-qubit gates in a brickwork pattern, each comprising single-qubit rotations uniformly distributed over the Bloch sphere (Haar-uniform unitaries) and a randomly directed controlled-NOT (CX) gate. In the measurement layer, measurements were placed independently on each qubit with probability p. These measurements were projective (σ^z) or null-type weak[21–23], the latter implemented by coupling the system qubit to an ancillary qubit through a unitary $V(\eta)$ before measuring the ancilla (Methods).

Weak-limit ($\eta = 0$) measurements do not affect the system, and $\eta = 1$ coincides with the projective limit, with intermediate η smoothly interpolating between the extremes. The particular structure of our circuits was designed to minimize circuit depth (Methods).

After the evolution was complete, we characterized the entanglement of the state by measuring Rényi entanglement entropies:

$$S_\alpha = \frac{1}{1-\alpha} \log_2 \left[\mathrm{Tr} \left(\rho_A^\alpha \right) \right], \qquad (1)$$

at order $\alpha > 0$, with the reduced density matrix ρ_A of a subsystem A recovered through quantum state tomography (QST) for each recorded trajectory defined by the mid-circuit measurement outcomes. The $\alpha = 1$ limit corresponds to the von Neumann entanglement entropy, $S_1 = -\mathrm{Tr}[\rho_A \log_2 \rho_A]$. Owing to the substantial cost of computing entanglement measures such as bipartite and tripartite mutual information, we characterized the transition through the mean entanglement entropy $\langle S_\alpha \rangle$ and variance $\mathrm{var}(S_\alpha)$, computed over the entanglement entropy values of each trajectory of each random circuit. A flowchart illustrating the experimental process is presented in Fig. 1d. The sampling process to acquire $\langle S_\alpha \rangle$ and $\mathrm{var}(S_\alpha)$ is resource-intensive, with an underlying exponential scaling in the number of mid-circuit measurements and in the subsystem size. On a circuit with m mid-circuit measurements, a total of 2^m distinct trajectories are possible, and a number of shots (repetitions) of the circuit scaling as 2^m is required to accumulate adequate copies of ρ_A in each trajectory for reliable tomography (Methods). To reduce the exponent in the exponential cost of tomography with the number of qubits in the subsystem $|A|$, we performed simultaneous tomography measurements on sets of mutually unbiased bases, which are groups of commuting Pauli strings of maximal size (Methods).

Entanglement crossover in the projective limit

The mean and variance of steady-state von Neumann entanglement entropy S_1 versus p on quantum hardware at system sizes $L = 4$, 5 and subsystem $|A| = \lfloor L/2 \rfloor$ under mid-circuit projective measurements are
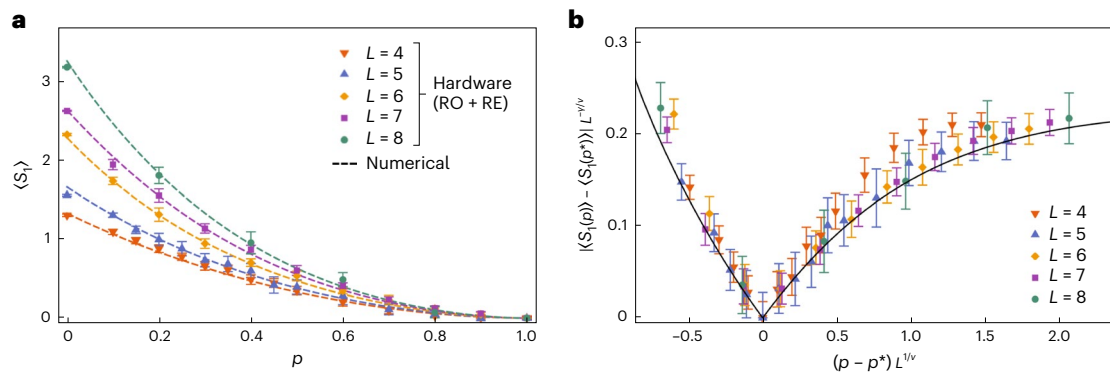
Fig. 4 | Phenomenological critical behaviour of the entanglement transition.
a, $\langle S_1 \rangle$ versus p under projective measurements for $4 \le L \le 8$ at subsystem sizes $|A| = \lfloor L/2 \rfloor$ obtained on quantum hardware with RO and RE applied. Dashed lines are ideal noiseless numerical results for comparison. **b**, Von Neumann entanglement entropies rescaled by a finite-size scaling form, showing a collapse of all data onto a single curve. A critical $p^* = 0.25$ is used, corresponding to the value at which the variance of S_1 exhibits a maximum that is indicative of a

crossover (Fig. 2d). Estimated best-fit critical exponents are $\gamma \approx 1.9 \pm 0.4$ and $v \approx 2.1 \pm 0.3$. Solid line shows noiseless numerical results at $L = 16$, with p and $\langle S_1 \rangle$ rescaled using best-fit (γ, v) from experiments for comparison. Quantum devices {ibm_lagos, ibm_perth, ibmq_jakarta, ibmq_casablanca} were used for $L \le 5$ and {ibm_hanoi, ibm_cairo, ibmq_kolkata} were used for $L > 5$. Error bars reflect 90% confidence intervals estimated from statistical bootstrapping.

shown in Fig. 2a–d. In Fig. 2a,b, we observe a monotonic decrease in $\langle S_1 \rangle$ with increasing p, consistent with the suppression of entanglement with increasing measurement rate. We note, however, that the raw experimental data consistently overestimate entanglement entropy due primarily to two sources: the misassignment of mid-circuit measurement outcomes due to readout error, and an effective decoherence-like effect, arising from gate errors averaged over the random circuits. To mitigate these non-idealities, we employed two error mitigation strategies. First, readout error mitigation reduces the effect of measurement bit-flip errors[42,43]. Second, a residual entropy correction was applied by noting that the entanglement entropy at $p = 1$ should vanish, but that detected on hardware is non-zero. An approximate correction was obtained by subtracting this residual entropy from all data at the same L, thus removing non-idealities from the detected entropy mean but leaving the variance unchanged (Methods).

With the readout error mitigation and residual entropy correction combined, the measured mean and variance of S_1 exhibit quantitative agreement with theory. In particular, in Fig. 2c,d a peak is evident in $\mathrm{var}(S_1)$ near $p \approx 0.25$, suggestive of a crossover between volume-law and area-law phases for $p < p^*$ and $p > p^*$, respectively. The quantitative agreement of the hardware data with theory supports the origin being an entanglement phase transition, as classical entropic contributions from hardware noise exhibit quantitatively different characteristics (Supplementary Note 7). We note that error bars and deviations from ideal noiseless numerics are more prominent at larger system size $L = 5$ than $L = 4$, a consequence of the deeper circuits and a reduced ability to avoid qubits with larger error rates.

Extensive and sub-extensive scaling of entanglement entropy

We now probe the scaling of steady-state entanglement entropy with system size, which exhibits distinct trends in the volume- and area-law entanglement phases. Taking $p = 0.1 < p^*$ below the crossover and $p = 0.8 > p^*$ above, we obtained hardware data on up to $L = 14$ qubits at subsystem sizes $|A| = L/4$. An interpolation between $|A| = \lfloor L/4 \rfloor$ and $|A| = \lceil L/4 \rceil$ was used in cases where L was not a multiple of four (Methods). These simulations were performed on 27- and 127-qubit quantum processors with sub-microsecond (~750 ns) readout and T_1, $T_2 \approx 100\ \mu\text{s}$ decoherence times. QST based on mutually unbiased bases, which is crucial for managing the resources needed for these experiments (Methods), in principle allows the recovery of the entanglement entropy at any order α. To demonstrate this flexibility, we report the

steady-state second-order Rényi entanglement entropy $\langle S_2 \rangle$ versus L in Fig. 2e. At $p = 0.1$, linear scaling of $\langle S_2 \rangle$ with L is evident; in contrast, $\langle S_2 \rangle$ scales sublinearly at $p = 0.8$, rapidly plateauing and becoming largely independent of L. We further remark that such scaling behaviour extends to all higher orders of entanglement entropy—as every $S_{\alpha>1}$ differs from S_∞ by at most a constant factor[17], they must all exhibit similar scaling with L. Additional hardware data at different α indeed show similar linear and sublinear scaling trends (Supplementary Note 6). The distinct scaling of entanglement entropy with system size, which matches quantitatively with theory, provides direct evidence of a volume- to area-law quantum phase transition realized on quantum hardware.

Entanglement crossover induced by weak measurements

Beyond projective measurements, we demonstrate an entanglement crossover using null-type weak measurements. Although weak measurements do not cause complete quantum state collapses, they nonetheless provide partial classical information on the measured system and can reduce entanglement entropy, likewise serving competitively against the evolving unitaries that generate entanglement. We report $\langle S_1 \rangle$ versus η in Fig. 3a,b for $p = 0.75$ and $p = 1$, respectively, at $L = 3$. These parameter sweeps represent horizontal slices of the p–η diagram of Fig. 1b, complementary to vertical slicing in the projective case. Only readout error mitigation was applied as cumulative hardware errors were sufficiently small to make residual entropy correction corrections negligible. At fixed p, $\langle S_1 \rangle$ decreases monotonically with η, as expected from the entanglement suppression of increasingly strong measurements. As shown in Fig. 3c,d, the signature peak in the entanglement entropy variance is likewise evident, marking a crossover between volume- and area-law phases. This crossover occurs at larger η when $p = 0.75$ than when $p = 1$, reflecting a trade-off between p and η necessary to cause a transition. Such a trade-off is also clear in Fig. 1b as the measurements depart from the projective limit.

In both projective (Fig. 2c,d) and weak measurement (Fig. 3c,d) experiments, we note slight deviations in entanglement entropy variance at large $p \gtrsim 0.9$ and $\eta \gtrsim 0.9$, where $\mathrm{var}(S_1)$ diminishes close to zero, but the error-mitigated hardware data do not decrease as steeply. We attribute this discrepancy to variations in hardware noise uncorrected by readout error mitigation and residual entropy correction, such as fluctuations in readout and coherent errors over the duration of the experiment, which manifest as an additional spread in the

measured entanglement entropy. We also note the poorer quality of the raw var(S_1) data in Fig. 3c,d, which exhibits flatter curves versus η in comparison with Fig. 2c,d. This difference is attributed primarily to differences in the quantum hardware, in particular, $\geq 1.5\times$ larger readout error rates on the devices used for weak measurement compared to $L \leq 5$ projective measurement experiments (Supplementary Note 7), and a larger number of qubits $2L = 6$ including ancillae.

Phenomenological critical behaviour of the transition

It is well-established in statistical mechanics that critical transitions are characterized by their scaling exponents, which also define universality classes. Here we utilized the large system sizes enabled by the hybrid quantum circuits to demonstrate that our observed crossovers exhibit the phenomenology of critical behaviour. This task was accomplished by performing a collapse of the measured entanglement entropy data onto a generic power-law scaling form. The specific form of the ansatz remains a topic of discussion and depends on the structure of the random circuits[14,16,18,44]. Assuming correlation length $\xi \approx |p - p^*|^{-\nu}$ and entanglement entropy $\langle S_\alpha \rangle \approx |p - p^*|^\gamma$, we took the finite-size scaling ansatz[45,46] to be:

$$|\langle S_\alpha(p) \rangle - \langle S_\alpha(p^*) \rangle| L^{-\gamma/\nu} = F'\left[(L/\xi)^{1/\nu}\right] = F\left[L^{1/\nu}(p - p^*)\right], \quad (2)$$

for unknown scaling functions F, F' and critical exponents γ, ν. Thus, upon appropriate rescaling by γ, ν, the measured entanglement entropy $|\langle S_\alpha(p) \rangle - \langle S_\alpha(p^*) \rangle|$ is expected to fall on the same curve for every L if the system exhibits critical behaviour. We report experimentally measured $\langle S_1 \rangle$ against p for $4 \leq L \leq 8$ in Fig. 4a. To perform the data collapse, we took $p^* \approx 0.25$, the location of the S_1 variance peak previously shown (Fig. 2d), for simplicity. We then obtained best-fit estimates of γ and ν (Methods). As shown in Fig. 4b, upon rescaling, the experimental data collapsed onto a single curve for values of $\gamma \approx 1.9 \pm 0.4$ and $\nu \approx 2.1 \pm 0.3$. A similar result was obtained when an extrapolation scheme to the thermodynamic limit was used to estimate $p^* \approx 0.22$, with nearly identical values of the γ, ν exponents. A qualitatively similar collapse occurred even with a weakened version of the residual entropy correction (Supplementary Note 5). We emphasize that the collapse procedure is dependent only on hardware-derived experimental data and operates entirely within the context of an arbitrary scaling function F, with no recourse to classical numerics, unlike in previous experimental studies of measurement-induced phase transitions.

We remark that finite-size effects, which manifest as L-dependent distortions from the scaling form, may affect the data collapse. We verified that the collapsed experimental data were consistent with numerics at a larger $L = 16$ (solid line in Fig. 4b). Further comparison of the critical behaviour of the transition against previous numerical studies is not straightforward owing to the different hybrid random circuits and the relatively small range of L used here. Reported values of p^* and critical exponents vary depending on circuit structure and scaling ansatz[14,16–18], and estimates from collapses of mutual information[19,24] differ from those of entanglement entropy. Nonetheless, the tight collapse of the hardware data at different L onto a single curve indicates that the phenomenology of critical behaviour has been observed, highlighting the self-consistency and fidelity of our quantum circuit executions.

Our results demonstrate that mid-circuit measurements can be effectively utilized to reduce quantum resource requirements, enabling the future exploration of dynamic quantum phases of matter on near-term quantum hardware. Future experimental studies of entanglement phase transitions may examine methods of characterizing the transition with reduced resource costs[34,47], for instance, by leveraging alternative exact or approximate protocols and entanglement measures that avoid exponential sampling costs[48,49]. Moreover, extensions of the paradigmatic random hybrid circuit model presently studied may harbour more intricate behaviour, such as an interplay

of topological and entanglement phase transitions[29,50], that could become accessible with $\geq 10^2$ mid-circuit measurements and $\lesssim 0.1\%$ two-qubit gate infidelities on hardware. More generally, mid-circuit measurements can reduce the resources required to prepare novel entangled quantum states of matter[29,50–52]. A number of questions, for instance concerning the universality classes of measurement-induced phenomena and a classification of quantum matter by their preparation and measurement complexity[53], remain open. Our work paves the way for the use of hybrid quantum circuits as an effective resource to investigate these phenomena and advance quantum simulations on near-term quantum hardware.

Online content

Any methods, additional references, Nature Portfolio reporting summaries, source data, extended data, supplementary information, acknowledgements, peer review information; details of author contributions and competing interests; and statements of data and code availability are available at https://doi.org/10.1038/s41567-023-02076-6.

References

1. Calabrese, P. & Cardy, J. Evolution of entanglement entropy in one-dimensional systems. *J. Stat. Mech. Theory Exp.* **2005**, P04010 (2005).
2. Kim, H. & Huse, D. A. Ballistic spreading of entanglement in a diffusive nonintegrable system. *Phys. Rev. Lett.* **111**, 127205 (2013).
3. Liu, H. & Suh, S. J. Entanglement tsunami: universal scaling in holographic thermalization. *Phys. Rev. Lett.* **112**, 011601 (2014).
4. Kaufman, A. M. et al. Quantum thermalization through entanglement in an isolated many-body system. *Science* **353**, 794–800 (2016).
5. Nahum, A., Ruhman, J., Vijay, S. & Haah, J. Quantum entanglement growth under random unitary dynamics. *Phys. Rev. X* **7**, 031016 (2017).
6. von Keyserlingk, C. W., Rakovszky, T., Pollmann, F. & Sondhi, S. L. Operator hydrodynamics, OTOCs, and entanglement growth in systems without conservation laws. *Phys. Rev. X* **8**, 021013 (2018).
7. Davies, E. B. & Davies, E. *Quantum Theory of Open Systems* (Academic, 1976).
8. Misra, B. & Sudarshan, E. C. G. The Zeno's paradox in quantum theory. *J. Math. Phys.* **18**, 756–763 (1977).
9. Wheeler, J. & Zurek, W. *Quantum Theory and Measurement* (Princeton Univ. Press, 1983).
10. Zhu, X. et al. Quantum measurements with preselection and postselection. *Phys. Rev. A* **84**, 052111 (2011).
11. Elliott, T. J., Kozlowski, W., Caballero-Benitez, S. F. & Mekhov, I. B. Multipartite entangled spatial modes of ultracold atoms generated and controlled by quantum measurement. *Phys. Rev. Lett.* **114**, 113604 (2015).
12. Dhar, S. & Dasgupta, S. Measurement-induced phase transition in a quantum spin system. *Phys. Rev. A* **93**, 050103 (2016).
13. Mazzucchi, G., Kozlowski, W., Caballero-Benitez, S. F., Elliott, T. J. & Mekhov, I. B. Quantum measurement-induced dynamics of many-body ultracold bosonic and fermionic systems in optical lattices. *Phys. Rev. A* **93**, 023632 (2016).
14. Li, Y., Chen, X. & Fisher, M. P. A. Quantum Zeno effect and the many-body entanglement transition. *Phys. Rev. B* **98**, 205136 (2018).
15. Chan, A., Nandkishore, R. M., Pretko, M. & Smith, G. Unitary-projective entanglement dynamics. *Phys. Rev. B* **99**, 224307 (2019).
16. Li, Y., Chen, X. & Fisher, M. P. Measurement-driven entanglement transition in hybrid quantum circuits. *Phys. Rev. B* **100**, 134306 (2019).
17. Skinner, B., Ruhman, J. & Nahum, A. Measurement-induced phase transitions in the dynamics of entanglement. *Phys. Rev. X* **9**, 031009 (2019).

18. Szyniszewski, M., Romito, A. & Schomerus, H. Entanglement transition from variable-strength weak measurements. *Phys. Rev. B* **100**, 064204 (2019).

19. Zabalo, A. et al. Critical properties of the measurement-induced transition in random quantum circuits. *Phys. Rev. B* **101**, 060301 (2020).

20. Nahum, A., Roy, S., Skinner, B. & Ruhman, J. Measurement and entanglement phase transitions in all-to-all quantum circuits, on quantum trees, and in Landau-Ginsburg theory. *PRX Quantum* **2**, 010352 (2021).

21. Gebhart, V. et al. Topological transition in measurement-induced geometric phases. *Proc. Natl Acad. Sci. USA* **117**, 5706–5713 (2020).

22. Zilberberg, O. et al. Null values and quantum state discrimination. *Phys. Rev. Lett.* **110**, 170405 (2013).

23. Wiseman, H. M. Quantum trajectories and quantum measurement theory. *J. Eur. Opt. Soc. Pt B* **8**, 205–222 (1996).

24. Lunt, O., Szyniszewski, M. & Pal, A. Measurement-induced criticality and entanglement clusters: a study of one-dimensional and two-dimensional Clifford circuits. *Phys. Rev. B* **104**, 155111 (2021).

25. Turkeshi, X., Fazio, R. & Dalmonte, M. Measurement-induced criticality in (2+1)-dimensional hybrid quantum circuits. *Phys. Rev. B* **102**, 014315 (2020).

26. Yu, X. & Qi, X.-L. Measurement-induced entanglement phase transition in random bilocal circuits. Preprint at https://arxiv.org/abs/2201.12704 (2022).

27. Tang, Q. & Zhu, W. Measurement-induced phase transition: a case study in the nonintegrable model by density-matrix renormalization group calculations. *Phys. Rev. Res.* **2**, 013022 (2020).

28. Turkeshi, X., Biella, A., Fazio, R., Dalmonte, M. & Schiró, M. Measurement-induced entanglement transitions in the quantum Ising chain: from infinite to zero clicks. *Phys. Rev. B* **103**, 224210 (2021).

29. Lavasani, A., Alavirad, Y. & Barkeshli, M. Measurement-induced topological entanglement transitions in symmetric random quantum circuits. *Nat. Phys.* **17**, 342–347 (2021).

30. Choi, S., Bao, Y., Qi, X.-L. & Altman, E. Quantum error correction in scrambling dynamics and measurement-induced phase transition. *Phys. Rev. Lett.* **125**, 030505 (2020).

31. Li, Y. & Fisher, M. P. A. Statistical mechanics of quantum error correcting codes. *Phys. Rev. B* **103**, 104306 (2021).

32. Fan, R., Vijay, S., Vishwanath, A. & You, Y.-Z. Self-organized error correction in random unitary circuits with measurement. *Phys. Rev. B* **103**, 174309 (2021).

33. Vasseur, R., Potter, A. C., You, Y.-Z. & Ludwig, A. W. W. Entanglement transitions from holographic random tensor networks. *Phys. Rev. B* **100**, 134203 (2019).

34. Bao, Y., Choi, S. & Altman, E. Theory of the phase transition in random unitary circuits with measurements. *Phys. Rev. B* **101**, 104301 (2020).

35. Jian, C.-M., You, Y.-Z., Vasseur, R. & Ludwig, A. W. W. Measurement-induced criticality in random quantum circuits. *Phys. Rev. B* **101**, 104302 (2020).

36. Sang, S. et al. Entanglement negativity at measurement-induced criticality. *PRX Quantum* **2**, 030313 (2021).

37. Block, M., Bao, Y., Choi, S., Altman, E. & Yao, N. Y. Measurement-induced transition in long-range interacting quantum circuits. *Phys. Rev. Lett.* **128**, 010604 (2022).

38. Gullans, M. J. & Huse, D. A. Dynamical purification phase transition induced by quantum measurements. *Phys. Rev. X* **10**, 041020 (2020).

39. Noel, C. et al. Measurement-induced quantum phases realized in a trapped-ion quantum computer. *Nat. Phys.* **18**, 760–764 (2022).

40. Córcoles, A. D. et al. Exploiting dynamic quantum circuits in a quantum algorithm with superconducting qubits. *Phys. Rev. Lett.* **127**, 100501 (2021).

41. Rost, B. et al. Demonstrating robust simulation of driven-dissipative problems on near-term quantum computers. Preprint at https://arxiv.org/abs/2108.01183 (2021).

42. Jurcevic, P. et al. Demonstration of quantum volume 64 on a superconducting quantum computing system. *Quantum Sci. Technol.* **6**, 025020 (2021).

43. Kandala, A. et al. Hardware-efficient variational quantum eigensolver for small molecules and quantum magnets. *Nature* **549**, 242–246 (2017).

44. Li, Y., Chen, X., Ludwig, A. W. W. & Fisher, M. P. A. Conformal invariance and quantum nonlocality in critical hybrid circuits. *Phys. Rev. B* **104**, 104305 (2021).

45. Fisher, M. E. & Barber, M. N. Scaling theory for finite-size effects in the critical region. *Phys. Rev. Lett.* **28**, 1516 (1972).

46. Binder, K. & Heermann, D. W. *Monte Carlo Simulation in Statistical Physics* 5th edn (Springer, 2010).

47. Gullans, M. J. & Huse, D. A. Scalable probes of measurement-induced criticality. *Phys. Rev. Lett.* **125**, 070606 (2020).

48. Li, Y., Zou, Y., Glorioso, P., Altman, E. & Fisher, M. Cross entropy benchmark for measurement-induced phase transitions. Preprint at https://arxiv.org/abs/2209.00609 (2022).

49. Lee, J. Y., Ji, W., Bi, Z. & Fisher, M. Decoding measurement-prepared quantum phases and transitions: from Ising model to gauge theory, and beyond. Preprint at https://arxiv.org/abs/2208.11699 (2022).

50. Sang, S. & Hsieh, T. H. Measurement-protected quantum phases. *Phys. Rev. Res.* **3**, 023200 (2021).

51. Tantivasadakarn, N., Thorngren, R., Vishwanath, A. & Verresen, R. Long-range entanglement from measuring symmetry-protected topological phases. Preprint at https://arxiv.org/abs/2112.01519 (2021).

52. Tantivasadakarn, N., Verresen, R. & Vishwanath, A. The shortest route to non-Abelian topological order on a quantum processor. Preprint at https://arxiv.org/abs/2209.03964 (2022).

53. Tantivasadakarn, N., Vishwanath, A. & Verresen, R. A hierarchy of topological order from finite-depth unitaries, measurement and feedforward. Preprint at https://arxiv.org/abs/2209.06202 (2022).

Methods

Quantum processors

We utilized IBM quantum devices supporting mid-circuit measurements in our experiments. For experiments with projective measurements at $L \leq 5$, we used 7-qubit devices ibm_lagos, ibm_perth, ibmq_jakarta, and ibmq_casablanca. For $L > 5$, we used 27-qubit devices, ibm_hanoi, ibm_cairo, ibmq_kolkata, ibm_auckland and a recent 127-qubit device, ibm_washington. This latter set of devices supports sub-microsecond readout, with typical readout times of ~750 ns, about twice as long as a CX gate and substantially faster than the ≥5 μs readout times on previous IBM devices. For experiments with weak measurements, we used the 16-qubit device ibmq_guadalupe and the 27-qubit device ibmq_montreal (ref. [42]). A summary of representative performance and noise characteristics on the quantum devices used is presented in Supplementary Table 3. To maximize experiment throughput, we ran parallel experiments where possible. To avoid qubits with large gate errors and to limit cross-talk, we ran at most two parallel circuits on sets of qubits separated by at least one idle qubit.

Weak measurements

We used null-type weak measurements[21,22], achieved by coupling the system qubit to an $|0\rangle$-ancilla through a unitary:

$$V(\eta) = e^{-ig(\mathbb{1}-\sigma^z)\otimes\sigma^y/2} = \begin{bmatrix} \mathbb{1} & 0 & 0 \\ 0 & \cos g & -\sin g \\ 0 & \sin g & \cos g \end{bmatrix}, \quad (3)$$

where $\sin^2 g = \eta$ and $\mathbb{1}$ is the 2×2 identity matrix. The effect of the coupling is:

$$\left(a|0\rangle + b|1\rangle\right)|0\rangle \rightarrow \left(a|0\rangle + b\sqrt{1-\eta}\,|1\rangle\right)|0\rangle + b\sqrt{\eta}\,|1\rangle|1\rangle. \quad (4)$$

In the $\eta = 0$ weak limit, the coupling $V(\eta) = \mathbb{1}^{\otimes 2}$, and the system and ancilla qubits remain fully separable. In the $\eta = 1$ projective limit, $V(\eta)$ is maximally entangling, and measuring the ancilla provides complete information on the system qubit. Intermediate strengths $0 < \eta < 1$ smoothly interpolate between these two extremes. The Kraus operators describing the measurement are:

$$M^+(\eta) = \begin{bmatrix} 1 & 0 \\ 0 & \sqrt{1-\eta} \end{bmatrix}, \quad M^-(\eta) = \begin{bmatrix} 0 & 0 \\ 0 & \sqrt{\eta} \end{bmatrix}. \quad (5)$$

Circuit optimizations

We applied several optimizations to the structure of our experiment circuits (Fig. 1c) to reduce circuit depth and complexity. First, due to qubit connectivity constraints on hardware, our circuits were set on open chains of L qubits instead of closed loops with periodic boundary conditions as in previous classical numerical studies[16,18,19]. Second, our randomized two-qubit gates each contained a single CX, in contrast with the 3 CXs required for general two-qubit operations, and on an individual level do not emulate Haar-uniform unitaries that have been used in previous studies[17,18,34]. We nonetheless note that, taken collectively, the brickwork pattern of our two-qubit unitaries does approximate Haar-uniformity (Supplementary Note 2). The numbers of time steps in experiment circuits were chosen to be sufficient to reach ≥95% of the steady-state entanglement entropy and ranged between ~1 and ~5 depending on L and p (Supplementary Note 1). The specific structure of our circuits, for instance with each time step comprising two brickwork layers of randomized two-qubit gates and a measurement layer, was chosen to minimize the number of time steps required to reach steady state.

An optimization to the decomposition of the coupling $V(\eta)$ in weak measurements was also used. An exact decomposition of $V(\eta)$ requires 2 CX gates. However, as our ancillary qubit was always initialized to $|0\rangle$,

it was necessary only for $V(\eta)$ to be exact in that sector. It was then possible to implement $V(\eta)$ with a single CX (Supplementary Fig. 1a,b). On circuits with multiple time steps, conditional resets[40] were used to re-initialize the ancilla to $|0\rangle$ after measurement, enabling reuse of the same set of ancillary qubits throughout the circuit. These resets operated by applying an X gate conditional on a computational-basis measurement.

Standard separable QST

To recover an n-qubit density matrix ρ through tomography, we employed projections onto all $2^n \times 3^n$ tensor products of n-qubit Pauli eigenstates, requiring 3^n quantum circuits each measuring a distinct Pauli string. This approach is referred to as standard separable QST, and has been shown to produce accurate tomography results compared with using non-overcomplete subsets of measurements[54,55]. To ensure physical ρ estimates, we employed least-squares linear inversion with constraints of Hermiticity, unity trace and positive semi-definiteness[56,57], instead of the computationally cheaper pseudoinverse.

QST with simultaneous measurements

At larger n, the number of tomography circuits and associated inversion costs can be greatly reduced by simultaneously measuring commuting Pauli strings[58,59]. In particular, every set of $4^n - 1$ non-trivial Pauli strings on n qubits can be partitioned into $2^n + 1$ groups, each containing $2^n - 1$ commuting strings. These groups are known as mutually unbiased bases (MUBs)[60]. To determine MUBs for tomography, we exhaustively enumerated clique covers of the commutation graph of the Pauli strings, first excluding the $\{\mathbb{1}, \sigma^x\}^{\otimes n}$, $\{\mathbb{1}, \sigma^y\}^{\otimes n}$ and $\{\mathbb{1}, \sigma^z\}^{\otimes n}$ qubit-wise commuting families. As the numbers and sizes of the cliques were fixed, the search procedure could be accelerated by recursion pruning, compared with the more general $\mathrm{MIN-CLIQUE-COVER}$ problem. The clique covers generated enumerated the subclass of MUBs with maximal fully separable basis sets[61], yielding at least three tomography circuits that required no two-qubit gates.

We used a stabilizer-based method to construct quantum circuits that implement MUB measurements[62], selecting the lowest-depth circuits after a transpilation process that replaced all SWAP gates with classical swapping of readout data. From the relative outcome frequencies of the n measurements on n qubits of each circuit, covering n Pauli strings, the expectation values of all $2^n - 1$ Pauli strings in the group could be recovered. Collecting $\langle\sigma^\mu\rangle_\rho$ for $\mu \in \{\mathbb{1}, x, y, z\}^{\otimes n}$, we assembled:

$$A\boldsymbol{\rho} = \mathbf{P}, \quad A = \begin{bmatrix} \mathbb{1}^{\otimes n} \\ \boldsymbol{\sigma}^{\mu_1} \\ \boldsymbol{\sigma}^{\mu_2} \\ \boldsymbol{\sigma}^{\mu_3} \\ \vdots \end{bmatrix}, \quad \mathbf{P} = \begin{bmatrix} 1 \\ \langle\boldsymbol{\sigma}^{\mu_1}\rangle_\rho \\ \langle\boldsymbol{\sigma}^{\mu_2}\rangle_\rho \\ \langle\boldsymbol{\sigma}^{\mu_3}\rangle_\rho \\ \vdots \end{bmatrix}, \quad (6)$$

for column-stacked vectorized density matrix $\boldsymbol{\rho}$ and Pauli operators $\boldsymbol{\sigma}^\mu$ row-wise flattened in A, such that the action of $\boldsymbol{\sigma}^\mu$ on $\boldsymbol{\rho}$ yielded $\mathrm{Tr}[\rho\sigma^\mu]$, and performed a least-squares linear inversion with Hermiticity, unity trace and positive semi-definiteness constraints to estimate ρ. We refer to this tomography strategy as MUBQST. Compared with standard separable QST, this approach yields significant savings in tomography costs with increasing n (Supplementary Table 1). For example, at $n = 4$, an almost five-fold reduction in the number of circuits is achieved. In our experiments, we used standard separable QST for $n \leq 2$ qubits, and MUBQST for $n > 2$ qubits.

Entropy mean and variance

An overview of the experimental methodology is presented in Fig. 1d. For a given p and η, a set of hybrid random circuits $\{c_i\}$ was first

generated, with each circuit defined by a list of gate angles and mid-circuit measurement locations. The structure of these circuits is shown in Fig. 1c. Each circuit c_i was executed repeatedly on a quantum device, yielding a mid-circuit measurement record (bitstring) and a tomography measurement bitstring for each shot. The former recorded measurement outcomes over the time steps of the circuit and distinguished the quantum trajectories realized on the device. We categorized the tomography measurement outcomes by their mid-circuit bitstrings, enabling the recovery of the subsystem density matrix and entanglement entropy of each trajectory—see above for details of the density matrix reconstruction. Mathematically, we acquired a set of mid-circuit bitstrings $\mathcal{R}_i$, with associated subsystem density matrix $\rho_A[r]$, entanglement entropy $S_\alpha[r]$ and relative frequency of occurrence $f[r]$ for each $r \in \mathcal{R}_i$. Finally, the entanglement entropy mean and variance were calculated over the set of sampled circuits $\{c_i\}$ and their trajectories as:

$$\langle S_\alpha \rangle = \frac{1}{|\{c_i\}|} \sum_i \sum_{r \in R_i} f[r] S_\alpha[r],$$

$$\text{var}(S_\alpha) = \frac{1}{|\{c_i\}|} \sum_i \sum_{r \in R_i} f[r] (S_\alpha[r] - \langle S_\alpha \rangle)^2. \tag{7}$$

We note that our methodology is akin to a sampling procedure, rather than strict post-selection—a fixed number of shots was executed for each circuit and the mid-circuit measurement records $\mathcal{R}_i$ sorted thereafter, instead of indefinitely executing shots until a specific mid-circuit record is found. This approach avoids data wastage. Owing to their lower hardware resource costs, for $L = 3$ with weak measurements and $L = 4, 5$ with projective measurements, we sampled ≥300 and ≥100 random circuits for each (p, η) data point, respectively; for all other L we sampled ≥50 random circuits per data point. There are ~10 MUBs for each sampled random circuit (Supplementary Table 1) and we executed ≥1,000 × 2^m shots per MUB for tomography, where m is the number of mid-circuit measurements in the circuit. Within an experiment, trajectories appearing with ≲100 total shots were discarded as they presented insufficient data for reliable tomography. The number of mid-circuit measurements m in the circuits ranged from ~4 to ~14 depending on L (Supplementary Table 2).

Subsystem size
To probe entanglement crossovers with projective and weak measurements (Figs. 2a–d and 3) and the criticality of the transition (Fig. 4), we used subsystem size $|A| = \lfloor L/2 \rfloor$. In probing the scaling of entanglement entropy with system size (Fig. 2e), however, we used quarter subsystem size $(A = L/4)$ to reduce the hardware resource costs in our experiments. To produce a smooth curve, we interpolated the value of $\langle S_2 \rangle$ between $|A| = \lfloor L/4 \rfloor$ and $|A| = \lceil L/4 \rceil$; no interpolation was used where L was a multiple of four and $\lfloor L/4 \rfloor = \lceil L/4 \rceil$. The alternate choice of only taking $|A| = \lfloor L/4 \rfloor$ introduces step-like patterns in $\langle S_2 \rangle$ versus L, but the key observation of extensive and sub-extensive scaling of entanglement entropy in the volume- and area-law phases is unchanged. Additional hardware data at $\alpha \in \{1, 3, 4\}$ exhibiting similar scaling trends are reported in Supplementary Note 6, using the same interpolation scheme.

Readout error mitigation
Measurement bit-flip error rates were acquired through calibration circuits run alongside experiments, and we performed least-squares linear inversion on raw measurement counts to approximately correct these errors[42,43]. In cases where only a subset of the n qubits was measured, occurring in $p < 1$ time steps and during QST on subsystems, the reduced calibration matrix was obtained by partial summation over qubits that were not measured. We used complete readout mitigation for $n \leq 5$ qubits, and tensored readout mitigation[56] for $n > 5$. The latter procedure calibrated qubit sub-registers in parallel, reducing the number of calibration circuits at the expense of neglecting correlations in the readout error between qubits in different sub-registers.

Residual entropy correction
On the random quantum circuits in our experiments, errors from the quantum gates are effectively averaged out into incoherent noise. Then, in the presence of hardware noise, the measured entanglement entropy is $S_\alpha = S_\alpha^* + \delta S_\alpha$, with S_α^* being the true value and δS_α arising from the combined decoherence. By taking $p = 1$ as the zero reference, we could calibrate the anomalous contribution δS_α and remove it from experimental data. To do so, we approximated that $\delta S_\alpha(p, \eta)$ scaled linearly with the error of quantum circuits c at p and η, $\langle \mathcal{E}[c_{p,\eta}] \rangle$, as calculated by composing reported gate-level error rates. The average was taken over all sampled circuits c for the experiment. The circuit error was estimated as:

$$\mathcal{E}[c] \approx \max_j \left(\varepsilon^{1q} N_j^{1q}[c] + \varepsilon^{2q} N_j^{2q}[c] + \varepsilon^{ro} N_j^{ro}[c] \right), \tag{8}$$

where $N_j^{1q}[c], N_j^{2q}[c], N_j^{ro}[c]$ are the number of one-qubit, two-qubit CX and measurement gates respectively in circuit c involving qubit j, and $\varepsilon^{1q}, \varepsilon^{2q}, \varepsilon^{ro}$ are one-qubit, two-qubit CX, and measurement error rates respectively, as reported in hardware calibration data. This linear scaling of $\delta S_\alpha(p, \eta)$ with circuit error is supported by characterization data (Supplementary Note 3). Note that c includes tomography gates and measurements, appended to the end of the experimental circuit.

The final quantum state should always be fully disentangled at $p = \eta = 1$, since all qubits are measured projectively at every time step. Any residual entanglement entropy detected must arise entirely from decoherent errors; that is, $S_\alpha(p = \eta = 1) = \delta S_\alpha(p = \eta = 1) \geq 0$. Thus, the anomalous entropy δS_α is related to the $\delta S_\alpha(p = \eta = 1) \geq 0$ reference as:

$$\delta S_\alpha(p, \eta) = \frac{\langle \mathcal{E}[c_{p,\eta}] \rangle}{\langle \mathcal{E}[c_{p=\eta=1}] \rangle} S_\alpha(p = \eta = 1). \tag{9}$$

Subtracting this correction from $S_\alpha(p, \eta)$ removes the anomalous entropy and provides a better estimate of the true entanglement entropy. Note there are no free parameters; in all experiments where residual entropy correction was applied, data for $S_\alpha(p = \eta = 1)$ were either part of the presented dataset or collected separately. The 7-qubit processors and the ≥27-qubit processors utilized in our experiments differed in their error characteristics. We took $\varepsilon^{1q} \approx 3 \times 10^{-4}$ and $\varepsilon^{2q} \approx 4 \times 10^{-3}$ for both families, but $\varepsilon^{ro} \approx 5 \times 10^{-3}$ for the former and $\varepsilon^{ro} \approx 8 \times 10^{-3}$ for the latter. These error rates reflect approximate values seen on the qubit chains picked by our selection algorithm and may not be representative of the average error on the processors. We also checked the robustness of our main results to data post-processing in Supplementary Notes 4 and 5, in particular using the trivial residual entropy correction scheme $\delta S_\alpha(p, \eta) = S_\alpha(p = \eta = 1)$ with no scaling corrections to entropic contribution from decoherence, in place of the linear scheme. Lastly, we remark that readout error mitigation and residual entropy correction play complementary roles in error mitigation, and residual entropy correction cannot subsume the task of the former. As residual entropy correction subtracts only an aggregate contribution $\delta S_\alpha(p, \eta)$ from $S_\alpha(p, \eta)$, the scheme cannot capture qubit and time variations in readout error characteristics; moreover readout errors affect $S_\alpha(p, \eta)$ in a qualitatively different manner to gate errors as they corrupt the mid-circuit measurement records (Supplementary Note 7). To maximize effectiveness, we employed residual entropy correction after readout errors were reduced by readout error mitigation.

Qubit selection
The quantum processors we utilized have more qubits than necessary for our experiments, thus presenting choices for the selection of qubits on which circuits are executed. We picked the set of qubits that minimized the estimated circuit error. Specifically, given the set $\mathcal{X}$ of qubit selections that satisfy connectivity constraints, we estimated the mean error:

$$\mathcal{E}_{x \in \mathcal{X}}[\mathcal{C}] = \sum_{j \in x} \left(\varepsilon_j^{1q} N_j^{1q}[\mathcal{C}] + \varepsilon_j^{2q} N_j^{2q}[\mathcal{C}] + \varepsilon_j^{ro} N_j^{ro}[\mathcal{C}] \right), \qquad (10)$$

where $\varepsilon_j^{1q}, \varepsilon_j^{2q}, \varepsilon_j^{ro}$ are one-qubit, two-qubit CX and measurement error rates, respectively, on qubit j, as reported in hardware calibration data. We selected the set of qubits x minimizing $\langle \mathcal{E}_x[\mathcal{C}] \rangle$, where the average was taken over the circuits to be executed, including their tomography components. We performed the minimization by an exhaustive search over the qubit connectivity graph of the processors. For weak measurements, qubits were selected to place an ancillary qubit adjacent to each system qubit (Supplementary Fig. 1c).

Collapse of hardware data

The data collapse procedure proceeded by way of numerical minimization of a measure of the scatter of data points, yielding the best-fit critical exponents γ, ν. The critical measurement rate p^* could either be determined separately or simultaneously with γ, ν in the collapse. We took $p^* \approx 0.25$ from hardware var(S_1) peak at $L = 5$ with projective measurements (Fig. 2d), as well as $p^* \approx 0.22$ from an extrapolation scheme into the thermodynamic limit (Supplementary Note 5) to check robustness. One complication is that the scaling function F, which sets the curve onto which the data collapses, is unknown, and the procedure must depend only on the experimental dataset[17,63,64]. To avoid preferential treatment of any portion of the data, we defined the measure of scatter symmetrically over each data subset[64]. We denote by $\mathcal{L}$ the set of system sizes in experiments, and $\mathcal{P}_L$ the set of sampled measurement rates p for each L. From experimental data $(p, \langle S_\alpha(p) \rangle)$ at $L \in \mathcal{L}$ and $p \in \mathcal{P}_L$, we computed the pairs $(q_L(p), W_L(p))$ rescaled as:

$$q_L(p) = (p - p^*) L^{1/\nu},$$
$$W_L(p) = (\langle S_\alpha(p) \rangle - \langle S_\alpha(p^*) \rangle) L^{-\gamma/\nu}, \qquad (11)$$

which follows from the finite-size scaling form in the main text. With the rescaled data at each L, we constructed a smoothed interpolating function $f_L(q)$, such that $f_L(q)$ gives the rescaled entanglement entropy W_L at each q_L. We denote the set of q_L as $\mathcal{Q}_L$, and $q_L^- = \min \mathcal{Q}_L$ and $q_L^+ = \max \mathcal{Q}_L$. Adapting the measure of goodness of fit from ref. 64, we define the loss function:

$$R(\gamma, \nu) = \sum_{L \in \mathcal{L}} \sum_{\substack{L' \in \mathcal{L} \\ L' \neq L}} L^{2\gamma/\nu} \sum_{\substack{q \in \mathcal{Q}_{L'} \\ q_L^- \leq q \leq q_L^+}} [f_L(q) - f_{L'}(q)]^2. \qquad (12)$$

The loss $R(\gamma, \nu)$ is a sum of squared residuals, measuring the scatter of rescaled data against the curve presented by the subset of data at each L. In assessing the scatter of the rescaled data, only data within a q interval overlapping with the considered curve are considered[17,64]; that is, $q \in [q_L^-, q_L^+]$. This procedure avoids extrapolation of $f_L(q)$. The prefactor of $L^{2\gamma/\nu}$ is for normalization after rescaling. The best-fit critical exponents are then $(\gamma_0, \nu_0) = \mathrm{argmin}_{\gamma, \nu} R(\gamma, \nu)$. Estimates of the fitting errors were set by the width of the minimum; for simplicity we considered the γ and ν parameters at the quadratic level[64]:

$$\delta\gamma^\pm = \epsilon\gamma_0 \left[2\ln \frac{R(\gamma_0 \pm \epsilon\gamma_0, \nu_0)}{R(\gamma_0, \nu_0)} \right]^{-1/2},$$
$$\delta\nu^\pm = \epsilon\nu_0 \left[2\ln \frac{R(\gamma_0, \nu_0 \pm \epsilon\nu_0)}{R(\gamma_0, \nu_0)} \right]^{-1/2}. \qquad (13)$$

In our analysis, we considered the four largest system sizes $\mathcal{L} = \{5, 6, 7, 8\}$ for which experimental data were available. These sizes were chosen to limit finite-size effects, which at small L caused deviations from the scaling form. To ensure the correct identification of the global minimum, a grid search followed by gradient descent was used. We report conservative estimates with lumped error $\gamma_0 \pm \max(\delta\gamma^+, \delta\gamma^-)$ and $\nu_0 \pm \max(\delta\nu^+, \delta\nu^-)$ at the $\epsilon = 1\%$ level, following ref. 64.

Numerics

Ideal noiseless numerical results presented throughout our study (black lines in Figs. 2–4) were computed on an independently sampled set of hybrid random circuits, using 50,000 realizations for each (p, η) data point. In each realization, a hybrid random circuit was constructed and the initial quantum state was exactly propagated over the unitary gates and measurements, in the process recording mid-circuit measurement outcomes and probabilities (using Born's rule). The circuits comprised ten time steps, more than sufficient to reach steady-state entanglement entropies even at the largest $L = 14$ system size investigated (see Supplementary Note 1 for minimum limits on time steps). Utilizing an independent set of circuits for numerics enabled a detection of sampling bias in our experimental circuits, in addition to assessing the agreement between hardware-measured entanglement entropy mean and variance and theoretical expectations.

Data availability

Data that support the findings of this study are publicly available via the Open Science Framework at https://osf.io/wkx49/.

Code availability

Code used in this study is publicly available via the Open Science Framework at https://osf.io/wkx49/.

References

54. Nielsen, E. et al. Gate set tomography. *Quantum* **5**, 557 (2021).
55. de Burgh, M. D., Langford, N. K., Doherty, A. C. & Gilchrist, A. Choice of measurement sets in qubit tomography. *Phys. Rev. A* **78**, 052122 (2008).
56. Aleksandrowicz, G. et al. Qiskit: an open-source framework for quantum computing. *Zenodo* https://zenodo.org/record/2562111 (2019).
57. Smolin, J. A., Gambetta, J. M. & Smith, G. Efficient method for computing the maximum-likelihood quantum state from measurements with additive Gaussian noise. *Phys. Rev. Lett.* **108**, 070502 (2012).
58. Hamamura, I. & Imamichi, T. Efficient evaluation of quantum observables using entangled measurements. *npj Quantum Inf.* **6**, 56 (2020).
59. Yen, T.-C., Verteletskyi, V. & Izmaylov, A. F. Measuring all compatible operators in one series of single-qubit measurements using unitary transformations. *J. Chem. Theory Comput.* **16**, 2400–2409 (2020).
60. Durt, T., Englert, B.-G., Bengtsson, I. & Życzkowski, K. On mutually unbiased bases. *Int. J. Quantum Inf.* **8**, 535–640 (2010).
61. Romero, J. L., Björk, G., Klimov, A. B. & Sánchez-Soto, L. L. Structure of the sets of mutually unbiased bases for *n* qubits. *Phys. Rev. A* **72**, 062310 (2005).
62. Gokhale, P. et al. Minimizing state preparations in variational quantum eigensolver by partitioning into commuting families. Preprint at https://arxiv.org/abs/1907.13623 (2019).
63. Serra, P. & Kais, S. Data collapse for the Schrödinger equation. *Chem. Phys. Lett.* **319**, 273–277 (2000).
64. Bhattacharjee, S. M. & Seno, F. A measure of data collapse for scaling. *J. Phys. A* **34**, 6375–6380 (2001).

Acknowledgements

Author contributions

J.M.K., S.-N.S. and A.J.M. conceived and initiated the project. A.J.M. supervised the project. J.M.K. developed the quantum simulation codebase and ran experiments on emulators and quantum hardware. M.M. contributed to the codebase and ran experiments on quantum hardware. All authors contributed to the discussion of results and writing of the paper.

Competing interests

The authors declare no competing interests.

Additional information

Supplementary information The online version contains supplementary material available at https://doi.org/10.1038/s41567-023-02076-6.

Correspondence and requests for materials should be addressed to Austin J. Minnich.

Peer review information *Nature Physics* thanks Daniel Sank and the other, anonymous, reviewer(s) for their contribution to the peer review of this work.

Reprints and permissions information is available at www.nature.com/reprints.